# Global 10-m impervious surface area mapping: A big earth data based extraction and updating approach

Zhongchang Sun [a,b,c], Wenjie Du [d], Huiping Jiang [a,b,*], Qihao Weng [e,*], Huadong Guo [a,b], Youmei Han [f], Qiang Xing [a,b], Yuanxu Ma [a,b]

[a] International Research Center of Big Data for Sustainable Development Goals (CBAS), Beijing 100094, China
[b] Key Laboratory of Digital Earth Science, Aerospace Information Research Institute (AIR), Chinese Academy of Sciences (CAS), Beijing 100094, China
[c] Key Laboratory for Earth Observation of Hainan Province, Hainan Research Institute, Aerospace Information Research Institute (AIR), Chinese Academy of Sciences (CAS), Sanya 572029, China
[d] School of Urban and Regional Science, East China Normal University, Shanghai 200241, China
[e] Department of Land Surveying and Geo-Informatics, The Hong Kong Polytechnic University, Hung Hum, Kowloon, Hong Kong, China
[f] School of Marine Technology and Geomatics, Jiangsu Ocean University, Lianyungang 222005, China

## ARTICLE INFO

## ABSTRACT

The impervious surface area is a critical component of anthropogenic environment that can be utilized as a proxy for assessing urbanization sustainability. However, there remains a lack of global high-precision product of impervious surface area, especially in the arid and semi-arid regions, due to the difficulty of human settlement extraction from remote sensing data. The complexity and variability of human settlements makes it difficult to identify and delineate impervious surfaces by using a single data source or classifier. In this paper, we employed Sentinel-1 synthetic aperture radar (SAR) and Sentinel-2 optical images, in conjunction with a range of ancillary datasets that were publicly available (such as nighttime light data and ecological zone information), to develop an accurate extraction and updating approach for global impervious surface area mapping across various geographical regions. We generated two high-resolution global impervious surface area (Hi-GISA) maps for 2015 and 2018 with the Google Earth Engine (GEE) platform. The resultant Hi-GISA maps not only provided a detailed distribution of human settlements in both urban and rural areas, but also helped quantitative change analysis in terms of both expansion and reduction. Conventionally, we randomly selected 3,980 and 4,354 blocks with a size of 300 m $\times$ 300 m for the respective datasets in 2015 and 2018, to compare the accuracy of our product with other products. The validation results show that the Hi-GISA data in each year reached a $R^2$ higher than 0.8 and achieved a mean overall accuracy over 88%. The areal estimations demonstrated that global impervious surfaces rose from 1.27 million $km^2$ in 2015 to 1.29 million $km^2$ in 2018 with an increase of 20,000 $km^2$. Nearly 80% of global impervious surfaces was contributed by 20 nations led by China, USA, and Russia. At the same time, South America had experienced the most significant growth ($\sim$3.35%) among all continents, followed by Africa ($\sim$2.59%). The Hi-GISA datasets provide new baseline products of global impervious surface area at 10 m resolution. These maps combined with other socioeconomic data could contribute to monitoring and analysis of the United Nations (UN) Sustainable Development Goals (SDGs), in particular, SDG 11.1, 11.2, and 11.3, and would also be valuable in assessing other SDG targets related to "Sustainable cities and communities". Further development of the Hi-GISA data with a longer time series could be potentially used to examine urban sprawl and its environmental impacts.

* Corresponding authors at: International Research Center of Big Data for Sustainable Development Goals (CBAS), Beijing 100094, China (H. Jiang). The Hong Kong Polytechnic University, Hung Hum, Kowloon, Hong Kong, China (Q. Weng).
*E-mail addresses:* sunzc@aircas.ac.cn (Z. Sun), 52213902014@stu.ecnu.edu.cn (W. Du), jianghp@aircas.ac.cn (H. Jiang), qihao.weng@polyu.edu.hk (Q. Weng), hdguo@radi.ac.cn (H. Guo), youmhan@jou.edu.cn (Y. Han), xingqiang@aircas.ac.cn (Q. Xing), mayx@aircas.ac.cn (Y. Ma).

## 1. Introduction

Our planet Earth has been urbanizing rapidly over recent decades. The proportion of world's population living in cities rises from 46.7% in 2000 to 55.3% in 2018, and it is anticipated to reach 60.4% in 2030 (UN, 2018). Meanwhile, fast urbanization causes resultant problems to human habitats, such as unplanned urban expansion, ground and air pollution, water shortages, inadequate infrastructure, urban–rural gap and so on (UN, 2017; Thomas et al., 2019). Well-managed urbanization, informed by a thoughtful understanding of long-term social, economic, and environmental trends, can help to maximize the benefits of agglomeration while minimizing ecosystem degradation and other potentially adverse impact amplified by an increasing number of urban dwellers. The UN thus proposes the Sustainable Development Goal 11

(SDG 11) aiming to bring about the sustainability of cities and other human settlements (UN, 2015). Particularly for SDG indicator 11.3.1 that is formulated by "the ratio of land consumption rate to population growth rate", it currently belongs to Tier II category, which means that the indicator is conceptually defined with established methodologies and available standards, but lacks regularly and normatively produced data by all countries (UN-Habitat, 2019). To this end, improved mapping of global impervious surface area is essentially needed to provide preliminary semantic information of human settlement to meet the SDGs, given that the impervious surfaces derived from satellite images can provide an accurate delineation of anthropogenic environment.

As more satellite remote sensing datasets are open, there has been increasing interest in impervious surface area mapping with a range of methods at various scales. These methods consist of decision tree (Weng

**Table 1**
Current mainstream medium and high-resolution long-term human settlement products.

| Name | Download URL | Producer | Definition | Resolution | Data source | Coverage |
|---|---|---|---|---|---|---|
| MODIS Land Cover Type Yearly Global 500 m (MCD12Q1 V6) | https://e4ftl01.cr.usgs.gov/MOTA/MCD12Q1.006/ | National Aeronautics and Space Administration | Built environment (>50%), including non-vegetated and human-constructed elements, with a minimum area > 1 km$^2$ | 493-m | MODIS 463-m data | Global |
| Global Human Settlement Layer (GHSL) | https://ghsl.jrc.ec.europa.eu/datasets.php | European Commission Joint Research Center | Human settlements and built-up layers (urban/rural) | 38-m | Global remote sensing data streams, census data, crowd or volunteered geographic information sources | Global |
| Global Land Cover Map (GlobCover V2) | https://dup.esrin.esa.int/page_globcover.php | European Commission Joint Research Center | Artificial surfaces and associated areas (urban areas > 50%) | 309-m | Envisat-MERIS | Global |
| National Land Cover Data (NLCD) | https://www.mrlc.gov/data?f%5B0%5D = category%3Aland%20cover | United States Geological Survey | Built-up areas and urban imperviousness | 30-m | Landsat data | USA |
| Corine Land Cover (CLC) | https://land.copernicus.eu/pan-european/corine-land-cover/ | European Commission Joint Research Center | Artificial surfaces and associated areas | 20-m | IRS Resourcesat 1/2, SPOT 4/5, RapidEye constellation | Europe |
| GlobeLand30 | https://www.globallandcover.com/defaults.html?src=/Scripts/map/defaults/download.html&head = download&type = data | National Geomatics Center of China | Artificial surfaces | 30-m | Landsat (TM5, ETM + ), HJ-1 | Global |
| Global Urban Footprint (GUF) | https://urban-tep.eu/puma/tool/?id = 567873922# | German Aerospace Center | Human settlements and built-up layers (urban/rural) | 12/84-m | TerraSAR-X data, TanDEM-X data | Global |
| Finer Resolution Observation and Monitoring-Global Land Cover (FROM-GLC) | https://data.ess.tsinghua.edu.cn/fromglc10_2017v01.html | Tsinghua University | Impervious surfaces | 10-m | Sentinel-2 data, FROM-GLC2015-v1 | Global |
| Normalized Urban Areas Composite Index (NUACI) | https://www.geosimulation.cn/GlobalUrbanLand.html | East China Normal University | Impervious surfaces | 30-m | Landsat data, DMSP-OLS 500-m data | Global |
| Global Artificial Impervious Area (GAIA) | https://data.ess.tsinghua.edu.cn/gaia.html | Tsinghua University | Impervious surfaces | 30-m | Landsat data, Sentinel-1 data, DMSP-OLS data | Global |
| Global Annual Urban Dynamics (GAUD) | https://figshare.com/articles/dataset/High_spatiotemporal_resolution_mapping_of_global_urban_change_from_1985_to_2015/11513178/1 | Sun Yat-Sen University | Impervious surfaces | 30-m | Landsat data, DMSP-OLS 500-m data | Global |
| Multisource, Multitemporal Random Forest (MSMT-RF) | https://doi.org/10.5281/zenodo.3505079 | Aerospace Information Research Institute, Chinese Academy of Sciences | Impervious surfaces | 30-m | Landsat-8 images, Sentinel-1 data, VIIRS NTL data, MODIS EVI imagery (MYD13Q1) | Global |
| Global Impervious Surface Area (GISA) | https://irsip.whu.edu.cn/resources/dataweb.php | Wuhan University | Impervious surfaces | 30-m | Landsat data | Global |
| ESA WorldCover | https://esa-worldcover.org/en | European Space Agency | Built-up land covered by buildings, roads, and other man-made structures with urban green (e.g., parks, sport facilities), waste dump deposits, and extraction sites excluded | 10-m | Sentinel-1 and 2 data | Global |
| ESRI Land Use/Land Cover | https://livingatlas.arcgis.com/landcover/ | Environmental Systems Research Institute | Built area including human made structures, major road and rail networks, and large homogenous impervious surfaces | 10-m | Sentinel-2 data | Global |

and Hu, 2008; Zhang et al., 2018; Wu et al., 2019), threshold-based segmentation (Xu et al., 2010; Liu et al., 2013; Wang et al., 2015; Deng and Wu, 2012), spectral mixture analysis (Wu et al., 2003; Civco et al., 2002; Li et al., 2013; Lu and Weng, 2004) and regression (Yang et al., 2003; Shao et al., 2015), among which the threshold-based segmentation method is considered a promising one with several advantages for large-scale operation and convenient implementation (Deng and Wu, 2012; Lu et al., 2014). Many satellite-derived products of impervious surface area or human settlement, which we consider to be two interchangeable jargons to delineate anthropogenic environment, have been generated during the last decade, although these products differ significantly in terms of spatiotemporal resolution and scale (Schneider et al., 2010; Xian and Homer, 2010; Pesaresi et al., 2013; Esch et al., 2013; Ban et al., 2015; Chen et al., 2015; Liu et al., 2018; Gong et al., 2019; Corbane, et al., 2019; Sun et al., 2019; Zhang et al., 2020; Huang et al., 2021), as displayed in Table 1. Among the existing products, Landsat imagery has proven to be one of the most optimal data sources to generate global products because of its long-term records since 1972, nearly global coverage, open access at 30 m resolution (Pesaresi et al., 2013; Chen et al., 2015; Liu et al., 2020; Yang and Huang, 2021). Despite reports that 30-m land cover products can provide sufficiently accurate information required for earth system modelling and land management analyses, the diversity and complexity of landscapes, as well as the similar spectral characteristics in optical imagery for different land cover types, can decrease the accuracy of impervious surface area identification (Sun et al., 2019). It seems to be problematic for dispersedly distributed human settlements located in *peri*-urban and rural regions, which are not included in most mainstream regional and global products. In addition, acquiring adequate high-quality optical images at low latitudes remains challenging due to the persistent cloudy weather, hindering the ability to monitor human settlement dynamics (Sun et al., 2019).

Since the synthetic aperture radar (SAR) remote sensing is supposed to be capable in observing land surfaces in all weathers, the SAR data can be used to overcome the limitation of optical images. The artificial landscape with high dielectric property and special geometric structure can cause intense backscattered echo in SAR images. Therefore, due to its sensitivity to agglomeration geometric aspects, SAR data can acquire vital information for cities. With the launch of high-resolution SAR satellites, these datasets can provide richer texture and shape features, and further delineate detailed information in urban areas (Esch et al., 2010, 2013, and 2017; Ban et al., 2015). At present, there are two representative products. The first one is a regional product from European Space Agency (ESA) in 2015 using the "KTH-Pavia Urban Extractor" (Ban et al., 2015). The Global Urban Footprint (GUF) is another well-known dataset from German Aerospace Centre based on TerraSAR-X (Esch et al., 2017). However, the previous studies mainly utilize the single-looking SAR data, which are inadequate for accurately mapping in urban areas, because the single-looking imaging will encounter problems like shadows and overlays that can impact the accuracy of human settlement extraction (Sun et al., 2019). To address such a deficiency caused by the usage of a single data source, integration of multisource data (e.g., optical and SAR images) is a promising solution (Weng, 2012; Sun et al., 2019).

Thanks to the disparities in methods, definitions, and satellite data that are used, various products of global impervious surface area show significant discrepancies, particularly true in arid, semi-arid, tropical, and sub-tropical regions, and for sparsely distributed human settlements with complicated landscapes, where accuracies are relatively lower (Gong et al., 2020; Liu et al., 2020), hence restricting the capacity for achieving a better understanding of worldwide urbanization process, especially for the monitoring and assessment of SDG 11 related indicators. At present, there still exist two major challenges for global impervious surface area mapping: (1) Spectral variations among similar land cover types complicate the identifying and extraction process; (2) Obtaining enough optical and SAR data with a specific time schedule

remains challenging. To overcome these limitations, we thus employed the integrated methods of threshold-based segmentation and change detection to create and update the high-resolution global impervious surface area (Hi-GISA) maps by fusing multi-orbit SAR data from Sentinel-1 (S1) and multitemporal optical data from Sentinel-2 (S2).

With the advent of various cloud computing platforms such as the Google Earth Engine (GEE), rapid and automatic mapping of large-area land covers becomes achievable (Cao et al., 2020; Ge et al., 2019; Wang et al., 2019). Meanwhile, the emerging big Earth data technology makes it possible to conduct the scientific synthesis and comprehensive application by combining all kinds of Earth observation data and geospatial information (Guo, 2017; Guo et al., 2020). Here we aimed to demonstrate the effectiveness of using a threshold segmentation procedure to extract the human settlements with complicated landscapes, and at the same time, we examined the reliability of applying a change detection approach to update the Hi-GISA data. To this end, we generated two new baseline 10-m products of global impervious surface area for 2015 and 2018 via the big Earth data technology and with the GEE cloud computing platform. We believed that these maps combined with other socioeconomic data might contribute to monitoring and assessment of the spatially relevant UN SDGs indicators such as SDG 11.3.1. On that basis, we also provided an alternative for global impervious surface area mapping and offered a fresh comprehension of quantitative estimation and spatially explicit distribution of global impervious surfaces at 10 m resolution.

## 2. Data

To improve the mapping performance in the middle-lower latitudes, we adopted the Interferometric Wide (IW) swath mode to derive a multi-look Ground Range Detected (GRD) product based on the double-polarized S1 SAR images (Sun et al., 2019). The calibrated, *ortho*-corrected S1 Level-1 GRD scenes at 10 m resolution are available for download on the GEE platform. We selected the scenes spanning from 2015 to 2018 for the generation of backscatter coefficient ($\sigma\circ$) in decibels (dB). We also downloaded the supplementary S2 Level-1C products from 2015 to 2016 as well as S2 Level-2A products for 2018. Subsequently, we employed four spectral bands, i.e., blue, green, red and near-infrared (NIR), from the acquired S2 data with less than 20% cloud cover. During the filtering process, the S2 Quality Assurance (QA) band was utilized to remove clouds and generate cloud-free images, and the nighttime light (NTL) images from the Visible Infrared Imaging Radiometer Suite (VIIRS) Day/Night Band (DNB) were employed to ensure the full coverage of intensive human activities. Besides, we utilized the Digital Elevation Model (DEM) data from Shuttle Radar Topography Mission (SRTM) to generate the slope images.

## 3. Methodology

In this study, we proposed a highly automated mapping procedure with human interactions on the GEE platform to develop global impervious surface area products at 10 m resolution for 2015 and 2018. There were six basic steps in the big Earth data based method: (1) Generate time series of backscatter coefficient ($\sigma\circ$) using the mean and standard deviation reduction factors to derive texture images; (2) Delineate potential impervious surface area based on the derived texture data; (3) Outline the built-up footprints utilizing the Normalized Difference Vegetation Index (NDVI) (Chen and Cihlar, 1996) and Normalized Difference Water Index (NDWI) (McFeeters, 1996); (4) Identify the optimal thresholds applying the "bimodal method" through strong bright/dark contrasts. (5) Enhance the mapping performances via the introduction of finer-scale global biome maps for arid and semi-arid areas (Olson et al., 2001), and considering the topographic factors in mountainous regions (Esch et al., 2010). (6) Derive the prospective expansion and reduction information through a change detection process between two different years. Here we employed a tailored change detection procedure to

update the Hi-GISA data for 2018 based on the baseline map of global impervious surface area for 2015.

### 3.1. Extraction method

The accuracy of impervious surface area mapping can be improved by combining multisource remote sensing time series. In this study, four satellite products of S1 SAR images, S2 optical images, SRTM DEM data and VIIRS NTL data were used collectively for extracting impervious surfaces. We followed the algorithm described in our previous studies to derive the initial impervious surfaces for 2015, given that the impervious surface area exhibited high-intensity brightness in SAR images (Sun et al., 2019). This method can accurately capture the spatial distribution information on impervious surface area by clearly masking out vegetation, water bodies, and bare lands. After excluding such background land cover types, we can identify these potential impervious surfaces (PIS) with complete and fine-scale boundaries, and a 3 pixels × 3 pixels majority filter was then performed to smooth the final classification results for 2015.

Worldwide human settlements with different landscapes have spectral similarities with other confusing land cover types. For instance, urban land and crop land have very similar spectral responses. Because of the considerable spectrum diversity, we cannot develop a universal classifier or gather a sufficient set of samples, which are applicable for operational global impervious surface area mapping (Chen et al., 2015). In this study, we reclassified the global landscapes with human settlements into eight representative sample areas and determined the empirical thresholds for each sample with specific characteristics. Tables 2 presents these features and typical examples in Google Earth imagery collected from eight sites all over the world.

We grouped multiple types of impervious surface area into different processing units according to their specific characteristics in SAR data (Table 2) and employed the corresponding input features for each unit to obtain the PIS. These input features included the following:

(1) $NDVI_{max}$: Annual maximum NDVI composite, generated from time series of S2 imagery;
(2) $MNDWI_{mean}$: Annual mean MNDWI composite, generated from time series of S2 imagery;
(3) $\sigma^{\circ}_{mean}$: Mean background coefficient generated from time series of S1 imagery;
(4) Slope: Extracted from SRTM DEM data;
(5) Vegetation Adjusted Normalized Urban Index (VANUI): Used to alleviate the effects of NTL saturation. The NTL and NDVI are combined in the VANUI defined as following (Zhang et al., 2013):
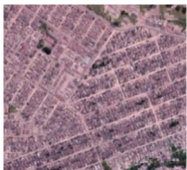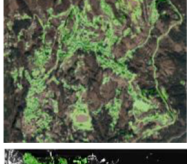
$$VANUI = (1 - NDVI) \times NTL \tag{1}$$

Fig. 1 presents examples for describing the extraction process. Here we show the difference between the single orbit and the fusion of double orbits of SAR data in Tehran, Iran for 2015 (Fig. 1**a, 1b, 1d, and 1e**). Shadows and overlaps have been nearly eliminated, and human settlement information in urban area is also enhanced. It is worth noting that the vegetation and bare rocks remain indistinguishable in optical images (Fig. 1**f**), which is a common situation for the classification in arid and semi-arid areas. Therefore, we further exclude areas with complex mountainous landforms by incorporating the DEM slope images (Fig. 1**c**). For the built-up areas spread out at low slopes, we can easily identify and extract the distinct human settlements from surrounding bare rocks due to their high scattering intensities in SAR images (Fig. 1**g**). Usually, a higher resolution mapping procedure provides better classification accuracies for scattered impervious surfaces (Fig. 1**i**).

### 3.2. Change detection

Due to the complex geomorphology and the complicated spectrum

**Table 2**
Input features for different impervious surfaces with various landscapes.

| ID | Impervious surface area | Input feature | Result |
|---|---|---|---|
| 1 | Dense urban area with features of high intensity SAR image | $NDVI_{max}$, $\sigma^{\circ}_{mean}$, |  |
| 2 | Scattered human settlements covered by dense vegetation with features of high intensity SAR image | $NDVI_{max}$, $\sigma^{\circ}_{mean}$, |  |
| 3 | Scattered human settlements surrounded by bare rocks and sand with features of high intensity SAR image | $MNDWI_{mean}$, $\sigma^{\circ}_{mean}$ |  |
| 4 | The strip-shaped residential areas and rough surface covered by trees showing strong SAR image features at the same time | $NDVI_{max}$ |  |
| 5 | Dense urban areas containing low-quality SAR image features, such as shadows and overlays ( e.g., skyscraper ) | $NDVI_{max}$, VANUI |  |
| 6 | Urban in high-slope mountainous areas showing strong SAR image features | $\sigma^{\circ}_{mean}$, $MNDWI_{mean}$, Slope |  |
| 7 | False positives in SAR images resulted from artificial buildings in water bodies (e. g., ships, steel facilities) | $\sigma^{\circ}_{mean}$, $MNDWI_{mean}$ |  |
| 8 | False positives in SAR images generated by agricultural lands (e.g., greenhouses) | $NDVI_{max}$ |  |

and spatial structure of the artificial land, for regions with different climate types (especially arid and semi-arid regions), it does cost much for threshold selection and manual editing to fix errors. Here we captured spatial changes in impervious surface area between 2015 and 2018 by adopting an improved update strategy with reference to the global baseline map for 2015. In consideration of the fact that impervious surfaces had strong scattering characteristics in SAR images, significant changes in scattering intensity caused by the expansion or reduction of human settlement can be identified. In addition, phenological features based on optical images, light data and SRTM topographic factors were also used to mask speckle noise and potential false positive objects (e.g., ships in water). After that, a 3 pixels × 3 pixels majority filter was utilized to eliminate the remaining noise and
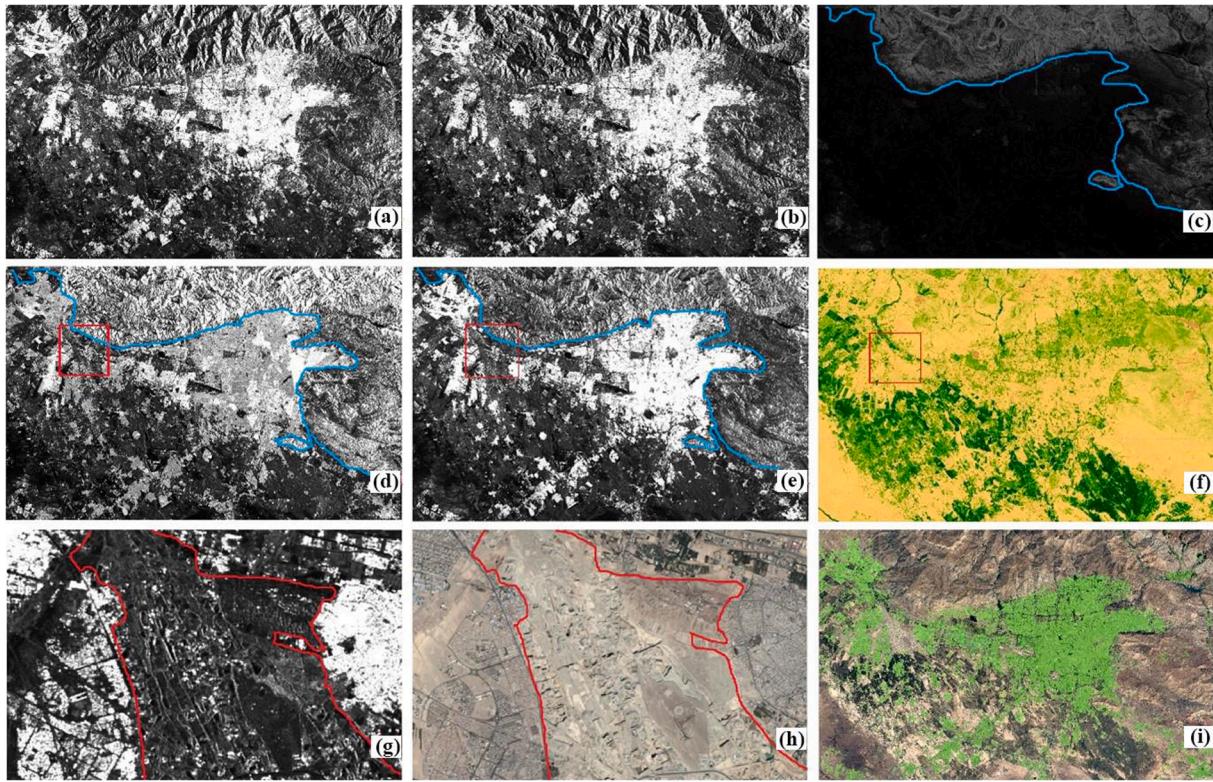
**Fig. 1.** Analyses of impervious surfaces in arid and semi-arid areas for 2015. (a) Up-track backscatter intensity; (b) Down-track backscatter intensity; (c) Slope; (d) Backscatter intensity calculated using the standard deviation; (e) Backscatter intensity calculated using the mean; (f) Maximum temporal Normalized Vegetation Difference Index (NDVI$_{max}$); (g) The backscatter intensity for a small region identified by the red rectangular inset in (e-f); (h) Google Earth image for the area shown in (g); (i) Final impervious surfaces, where the green layer represents the mapping product.

geometric errors resulted from edge dislocation when combining SAR images. Finally, potential changes in impervious surface area were extracted to derive the new global map for 2018. Fig. 2 illustrates the processing flow chart.

In this study, we extracted the potential expansion (PIS1$_{in}$) or reduction (PIS1$_{de}$) between 2015 and 2018 using the backscattering coefficients of SAR images to obtain the impervious surface area changes:

$$PIS1_{in} = (PIS1_{18} = 1) and (PIS1_{15} = 0) \tag{2}$$

$$PIS1_{de} = (PIS1_{18} = 0) and (PIS1_{15} = 1) \tag{3}$$

where PIS1$_{15}$ and PIS1$_{18}$ are the potential impervious surfaces derived from the backscattering coefficients for 2015 and 2018, respectively.

When extracting impervious surface area changes from SAR images using backscattering coefficients, it is easy to miss residential pixels with darker counterscatter values. To this end, we identified the texture features of angular second moment, entropy and contrast in SAR images using the gray-level co-occurrence matrix, which are effective indicators for the texture measurements of urban lands to supplement the backscattering coefficients (Esch, et al., 2013). The window sizes that should be compatible with the image resolution were selected as 3 pixels × 3 pixels and 9 pixels × 9 pixels (Zhang et al., 2014). The three texture features were thresholded and then a logical operation was performed to obtain the potential impervious surfaces (PIS2):

$$PIS2 = (Asm < T_3) or (Ent > T_4) or (Con > T_5) \tag{4}$$

where T3, T4, and T5 are the empirical thresholds of angular second moment (Asm), entropy (Ent) and contrast (Con), respectively. After repeated experiments, T3 was set to 1, T4 was set to 0.6, and T5 was set to 0.32 in this study.

Similarly, calculations were also performed based on the potential impervious surfaces extracted from SAR image texture features for 2015 and 2018, so as to capture the prospective impervious surface changes including expansion changes (PIS2$_{in}$) and reduction changes (PIS2$_{de}$):

$$PIS2_{in} = (PIS2_{18} = 1) and (PIS2_{15} = 0) \tag{5}$$

$$PIS2_{de} = (PIS2_{18} = 0) and (PIS2_{15} = 1) \tag{6}$$

where PIS2$_{15}$ and PIS2$_{18}$ are the potential impervious surfaces based on SAR image texture feature extraction for 2015 and 2018, respectively.

Next, the impervious surface changes extracted based on the backscattering coefficients (PIS1$_{in}$/PIS1$_{de}$) and those extracted based on the SAR image texture features (PIS2$_{in}$/PIS2$_{de}$) were jointly used to generate the improved results of potential expansion (PIS$_{in}$) or reduction (PIS$_{de}$) between 2015 and 2018:

$$PIS_{in} = (PIS1_{in} = 1) or (PIS2_{in} = 1) \tag{7}$$

$$PIS_{de} = (PIS1_{de} = 1) or (PIS2_{de} = 1) \tag{8}$$

Meanwhile, the spectral and texture features of the optical images were used to mask vegetation and waters before further detecting potential changes of impervious surface area. The existing studies have shown that vegetation growing seasons are the best time to extract the distribution information of impervious surfaces in temperate continental climate zones, and the same to dry seasons in subtropical monsoon regions (Sun et al., 2019; Zhang et al., 2020). When S1 SAR data is combined with S2 opotical data, we can effectively capture the interannual variation of impervious surface area that is different from other land cover types. Besides, we also employed multitemporal lifting orbit image fusion to interpolate the shadowed and saturated pixels in densely built areas.
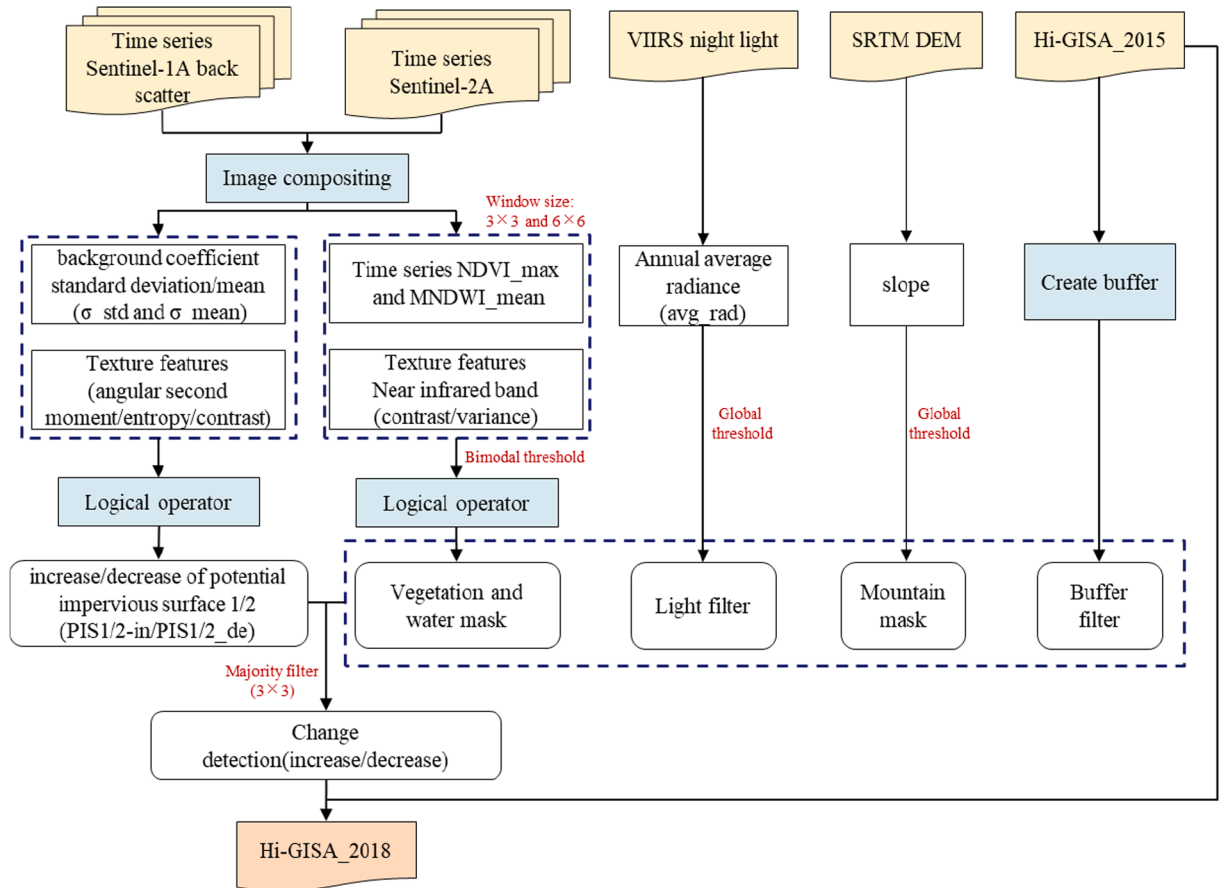
**Fig. 2.** Flow chart of global impervious surface mapping for 2018 based on 2015.

According to our previous research (Sun et al., 2019), the maximum value of the NDVI and the mean value of the NDWI can be selected as the appropriate thresholds to remove the misclassification resulted from rough vegetation and bright scatterers in water bodies. The two indices are calculated as follows:

$$NDVI_{max}(T) = max(NDVI)_\alpha^\beta \tag{9}$$

$$MNDWI_{mean}(T) = (MNDWI)_\alpha^\beta mean \tag{10}$$

where $NDVI_{max}$ and $MNDWI_{mean}$ are the maximum composite NDVI and the mean composite MNDWI from S2 acquisitions, respectively; $T$ denotes the spanning time period; $\alpha$ and $\beta$ are the foremost and the last scenes acquired in the given time period.

The local texture measurements for S2 optical images were used to constrain the impacts of the bright scatterers in the vegetation and water bodies on the extraction results. Because there are redundancies and similarities in texture features among the S2 data in different time periods, only the variance (Var) and contrast (Con) textures of the near-infrared band from the local windows of 3 by 3 pixels and 9 by 9 pixels were used in this study (Chen et al., 2015). For expansion detection, texture features in 2018 were used as constraints; and for reduction detection, texture features in 2015 were used as constraints. Through trial and error, the empirical variance threshold ($T_{var}$) and contrast threshold ($T_{con}$) of Sentinel-2 images were both set to 3. The pixels with variance>3 and contrast over 3 were deemed to be potential human settlements in the Sentinel-2 images.

The SAR images show bright scattering characteristics on bare rocks and rough surfaces, such as mountain folds and deserts, which cannot be distinguished through optical phenological features as well. Therefore, multitemporal VIIRS nightlight data from 2015 were introduced to assist with the identification process. The reasonable buffer zone (2 km) established based on the global 10-m impervious surface area product in 2015 further constrained the extent of urban expansion or reduction. The potential impervious surface changes using the backscattering co-efficients and texture features of SAR images were subjected to these constrains to create the final impervious surface change information between 2015 and 2018. Logical operations were then used to generate the output for a grid of 5° × 5° in latitude and longitude to obtain the global impervious surface area product at 10 m resolution for 2018.

*3.3. Post-editing*

The post-editing step was finally conducted to eliminate false alarms in the consequent Hi-GISA layers. The pixels were identified and reassigned if their zonal statistics regarding the maximum value of the NDVI ($NDVI_{max}$) indicated an erroneous assignment as natural surface area while the mean value of the NDVI ($NDVI_{mean}$) indicated an opposite assignment as impervious surface area (e.g., the vegetation covered areas in Northern Italy). When this was the case, objects would have a high $NDVI_{max}$ (>0.6), a low $NDVI_{mean}$ (less than0.2) and a high value for the mean temporal SAR backscatter intensity ($\sigma°_{mean} > 0.1$). Other typical false alarms occurred when the maximum temporal NDVI was too high, especially in the plain areas of America or Southern Italy, and when the temporal SAR backscatter intensity was too low, for example, in the highly textured rice fields. These misclassifications can be accurately identified and reasonably corrected via post-editing. An exemplary case for the rule-based amendments of false alarms is shown in Fig. 3, where we substituted the $NDVI_{max}$ (Fig. 3a) with $NDVI_{mean}$ (Fig. 3b) to conduct the vegetation filtering.
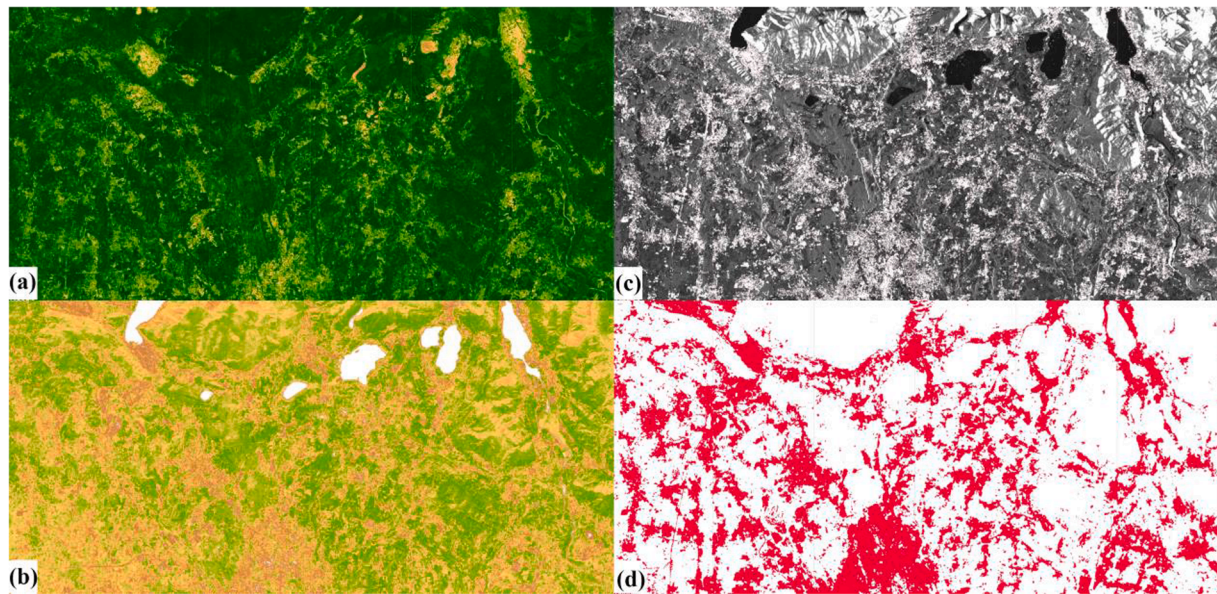
**Fig. 3.** A post-editing example for rule-based amendments in the south piedmont of the Alps in Northern Italy. (a) The maximum temporal NDVI for 2015; (b) The mean temporal NDVI for 2015; (c) The mean temporal backscatter for 2015; (d) The amending result for 2015.

### 3.4. Accuracy assessment

In this study, we employed two different methods to evaluate the mapping accuracies of impervious surfaces and compare their performances with other existing products that have been extensively applied in urbanization studies. For the global map of 2015, massive validation points with a size of 10 m × 10 m were randomly generated covering the geographical regions of Europe, Africa, North America, South America, and Oceania. It should be noted that we carried out the validation process via visual interpretation with reference to high-resolution Google Earth images. At the same time, a uniform interpretation rule was formulated to produce the reference data (Sun et al., 2019). The extraction results and reference data were used to develop confusion matrix for each geographical region. We further calculated the indicators of user's accuracy (UA), producer's accuracy (PA), and overall accuracy (OA) to evaluate the mapping accuracy. To facilitate a reliable comparison among different global maps, we further generated 3,980 and 4,354 random blocks of 300 m × 300 m for 2015 and 2018, respectively (Fig. 4). For each block, impervious surfaces were visually interpreted against the corresponding high-resolution Google Earth images, and the proportion of artificial lands was computed to generate the reference data. We mainly implemented the cross-product comparisons among the datasets of GAIA from Gong et al. (2020), NUACI from Liu et al. (2018), GHSL, ESA, ESRI, CLC, and NLCD. After calculating the coverage percentage of impervious surfaces in each block for respective maps, the determination coefficient ($R^2$) between different products and the reference data based on scatter plots was used to complement the accuracy assessment (see Fig. 5).
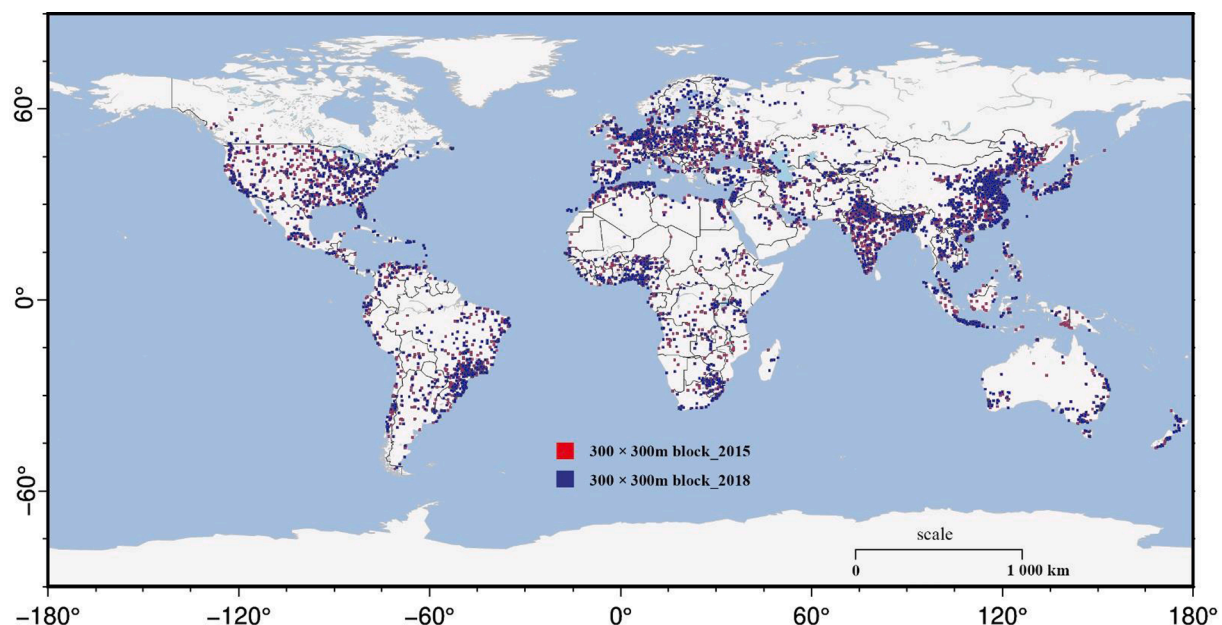


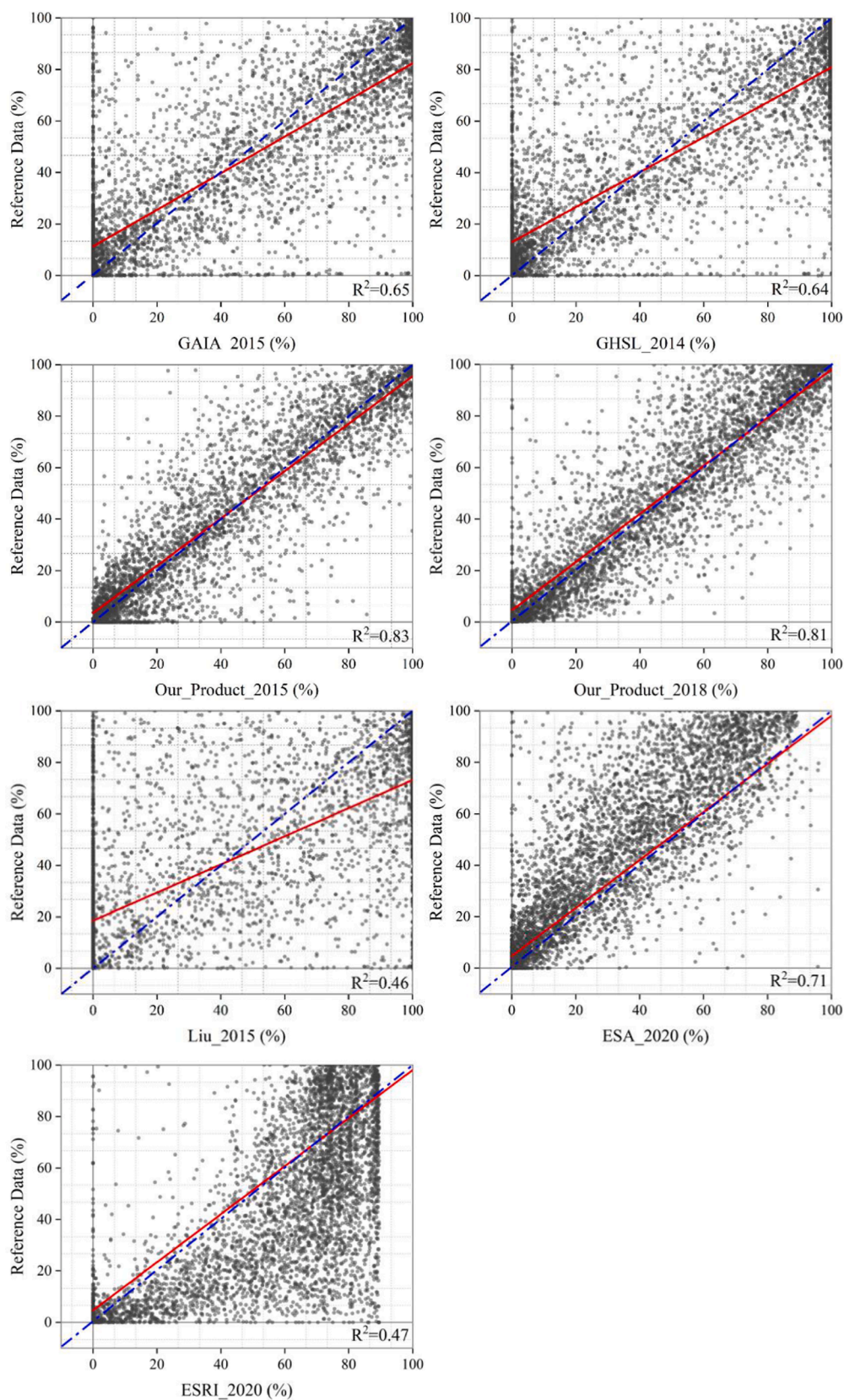**Fig. 4.** Global validation blocks of 300 m × 300 m for 2015 and 2018.

**Fig. 5.** Scatter plots representing the estimation against reference of impervious surface area percentage for all validation blocks in different global maps.

# 4. Results and analysis

## 4.1. Mapping validation

The detailed results of accuracy assessment about the Hi-GISA data in 2015 are shown in Table 3. Globally for this map, the indicators of OA and overall kappa were 88.99% and 0.7808, respectively, while the indicators of PA and UA were 95.52% and 83.45%, respectively. Overall, no significant differences were found between various geographical regions. For example, the validation results showed that Asia was slightly more accurate than Africa. Specifically, OA, PA, UA were 88.55%, 94.58% and 81.81% for China, and the accuracies varied from province to province with the arid and semi-arid areas showing the worst performances (Sun et al., 2019). According to the results revealed by the scatter plots, our products demonstrated a better fit with the reference data than other urban land cover products across different geographical regions (Fig. 6). Except for CLC in Europe and NLCD in North America, our global impervious surface area maps reached the highest values of $R^2$. In summary, Hi-GISA 2015 had the highest $R^2$ (0.83) followed by Hi-GISA 2018 (0.81), ESA 2020 (0.71), GAIA 2015 (0.65), GHSL 2014 (0.64), ESRI 2020 (0.47), and NUACI 2015 (0.46), indicating that our results yielded a more fitted regression with the reference data. It should be noted that the spatial resolutions of remote sensing data sources seemed to have no impact on whether the corresponding satellite-derived global impervious surface maps could achieve high accuracies, given that the Hi-GISA, ESA, and ESRI datasets were generated based on the same 10-m Sentinel imagery while the GAIA, GHSL, and NUACI datasets were generated based on the same 30-m Landsat imagery, but their performances differed significantly in terms of mapping validation. To our knowledge, the mapping methods might play a decisive role in determining the accuracies of final products, although the spatial resolution of satellite imagery is also an important influencing factor.

## 4.2. Mapping performance and spatial variations

In terms of mapping performance, regional impervious surface mapping results were produced for the basic year of 2015 with China, USA, and Europe serving as examples in binary images (Fig. 7). The red patches represented impervious surfaces while the white ones indicated the permeable surface area. Apparently, most of the urban agglomerations located in areas with the best geographical advantages, such as seaside and plains. The 2015 product provides spatially explicit information about the distribution of human settlement, specifically accurate and detailed boundaries between urban and rural impervious surface area, which can provide insights into fine-scale urban–rural planning and management.

We compared six representative impervious surface areas from four different natural backgrounds to examine their spatial variation derived from different products (Fig. 8). These areas range from urban agglomerations to small rural settlements, and they are each illustrated in S2 (2018) true color composite images, Hi-GISA (2018), GAIA (2018), FROM-GLC (2017), GHSL (2014), NAUCI (2015), ESA (2020), and ESRI (2020) maps. For the figures in columns 2–8, human settlements are represented in red. Four typical arid areas with impervious surfaces

were selected to compare the extraction accuracies and distribution details of different products (Fig. 8, **rows 3**–**6**), including the slum districts and industrial areas on flat bare rocks in Morbi, India, the high-density city of Dubai, UAE that was located in a vast desert, small scattered residential areas in valley folds (e.g., Shannan, China), and settlements distributed on flat bare lands (e.g., Yinchuan, China). Other regions with dense vegetation were also selected to assess the identification capacity of scattered settlements, including dense rural settlements in plains (e.g., Johannesburg, South Africa), and scattered high-grade residential areas in the plain basins (e.g., Chicago, USA).

For semi-arid city clusters (Fig. 8, **Row 1**), the classifications from FROM-GLC and ESA provided a general outline of human settlements, but failed to identify impervious surfaces with considerable green spaces. This omission possibly came from a lack of adequate training samples (Zhang et al., 2020). Conversely, the GHSL, GAIA, NUACI and ESRI products tended to overestimate urban expansions for forming a continuous distribution pattern. Only the classification from Hi-GISA delineated a fine-scale distribution of human settlements with relatively accurate boundaries that conformed to the visual interpretation results. For the human settlements concentrated in the plain areas (Fig. 8, **Row 2**), high-grade residential districts scattered on the urban fringe, and such areas were densely distributed and connected by complex road networks. The NUACI data showed good accuracies in the city center but missed narrow roads. GHSL and GAIA wrongly separated these scattered settlements into isolated spots while Hi-GISA, FROM-GLC, and ESA preserved narrow roads without loss of details and performed well either in urban or *peri*-urban area.

For cities growing on bare rocks (Fig. 8, **Row 3**), scattered human settlements were connected by narrow roads. ESRI, NUACI, and FROM-GLC had varying degrees of overestimation due to the misclassification of bare lands into impervious surfaces in the suburb. ESA, GHSL and GAIA failed to extract small villages in *peri*-urban areas. For cities in the desert that was mostly covered by coarse sand and gravels (Fig. 8, **Row 4**), GAIA and GHSL missed most of road networks as well as sparsely distributed settlements on the urban fringe. FROM-GLC and NUACI displayed more spatial details of impervious surfaces but discarded small settlements. Comparatively, the Hi-GISA and ESA data provided an unbiased delineation for urban and *peri*-urban features at a higher resolution.

In high-altitude regions, the landscape was characterized by compact settlements intermixed with vegetation and water bodies (Fig. 8, **Row 5**). For these settlements, Hi-GISA and ESA not only provided an accurate identification, but also gave a clear distinction from other land covers. GAIA can only capture the core urban area while FROM-GLC and ESRI misclassified bare rocks and shadows both in urban and *peri*-urban areas. Both of NUACI and GHSL failed to give a classification in this kind of region. The areas with complicated environmental backgrounds such as bare soils and mixed farmlands are shown in Fig. 8, **Row 6**. As we can see, there were also dense industrial sheds and greenhouses near the core urban area. For these features, the Hi-GISA and FROM-GLC products performed well, and they can even capture more details about paths and small buildings around the greenhouses. GAIA and ESA had the best extraction performances of industrial sheds, but small roads and greenhouses seemed to be abandoned largely. NUACI underestimated in the urban core while GHSL failed to identify the surrounding rural settlements and roads. Meanwhile, ESRI tended to overestimate the human settlements, which was the same as above.

## 4.3. Quantitative description of Hi-GISA

Over the past few decades, the total area of impervious surfaces in Asia has been rising at an alarming rate with the highest average annual growth (Gong et al., 2020). Between 2015 and 2018, the growth rates of impervious surfaces in South America and Africa were 3.35% and 2.59%, respectively, surpassing the rate in Asia (1.38%) (Fig. 9a). For Europe and Oceania, the growth rate of impervious surfaces was less

**Table 3**

Accuracies of impervious surface maps across different validation regions for 2015.

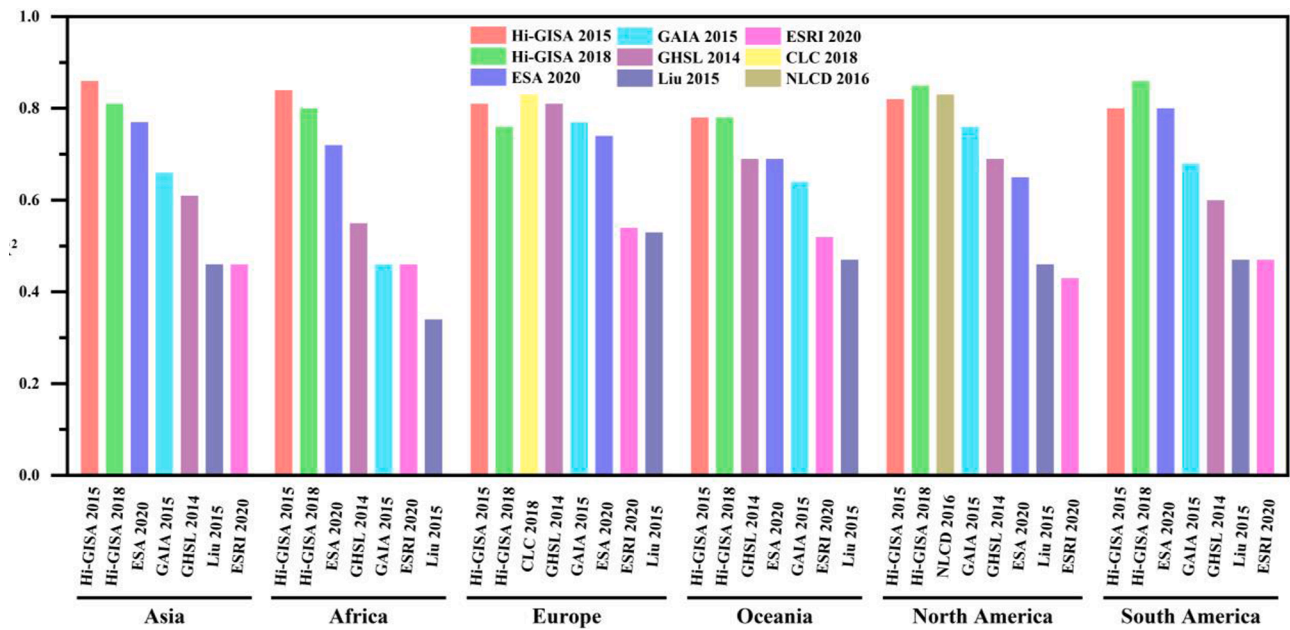| Region | Sample size | OA (%) | UA (%) | PA (%) |
|---|---|---|---|---|
| Asia | 256,593 | 88.86 | 82.94 | 95.53 |
| South America | 36,556 | 89.94 | 83.61 | 98.51 |
| Oceania | 22,012 | 89.31 | 84.29 | 94.89 |
| Africa | 32,493 | 88.77 | 86.00 | 92.27 |
| Sum/Average | 347,654 | 88.99 | 83.21 | 95.52 |

**Fig. 6.** Comparisons of $R^2$ in different global maps grouped by geographical regions.
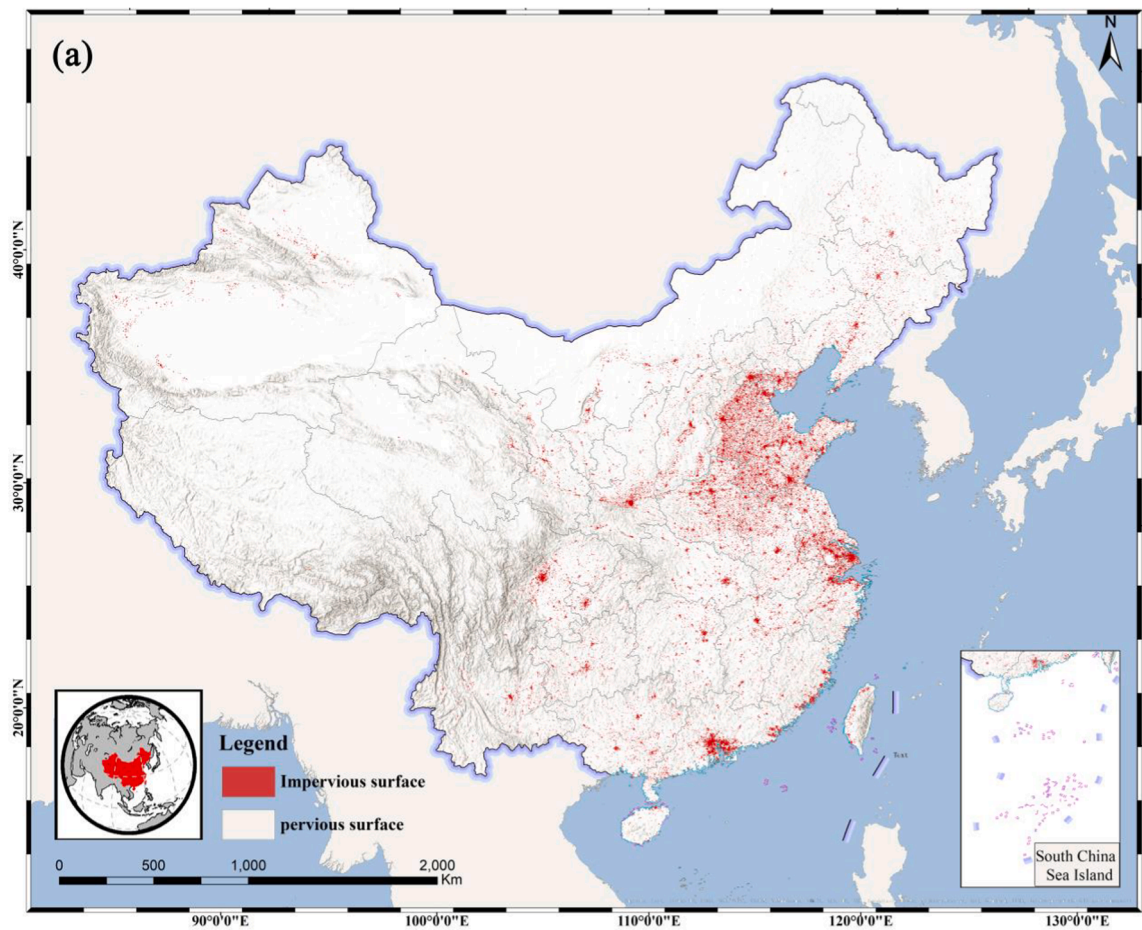


**Fig. 7.** Overviews of Hi-GISA products for 2015 in China, USA, and Europe, respectively.
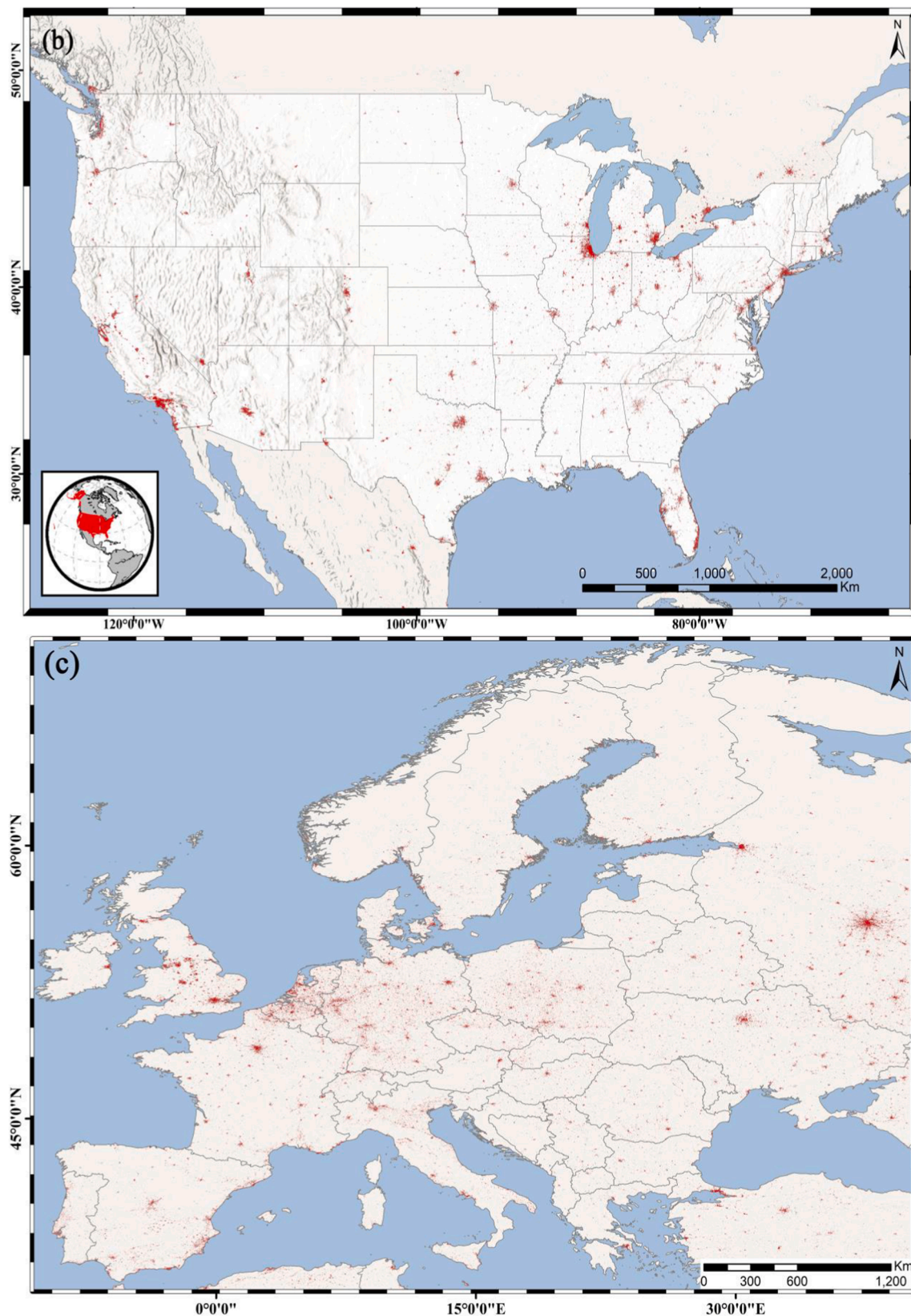
**Fig. 7.** (*continued*).

than 0.5%; and for North America, the rate was close to 1%. This change in trend reveals the unprecedented sprawl of cities in South America and Africa in recent years. The global fraction of impervious surfaces in North America was close to that in Europe (~20%) in 2018. During the period 2015–2018, Asia was dominantly the leader in terms of artificial land expansion, the impervious surfaces in Asia accounted for ~ 46% of the total areas (Fig. 9b). Specifically, the total area of impervious surfaces in Asia increased from 589,011 km$^2$ in 2015 to 597,145 km$^2$ in
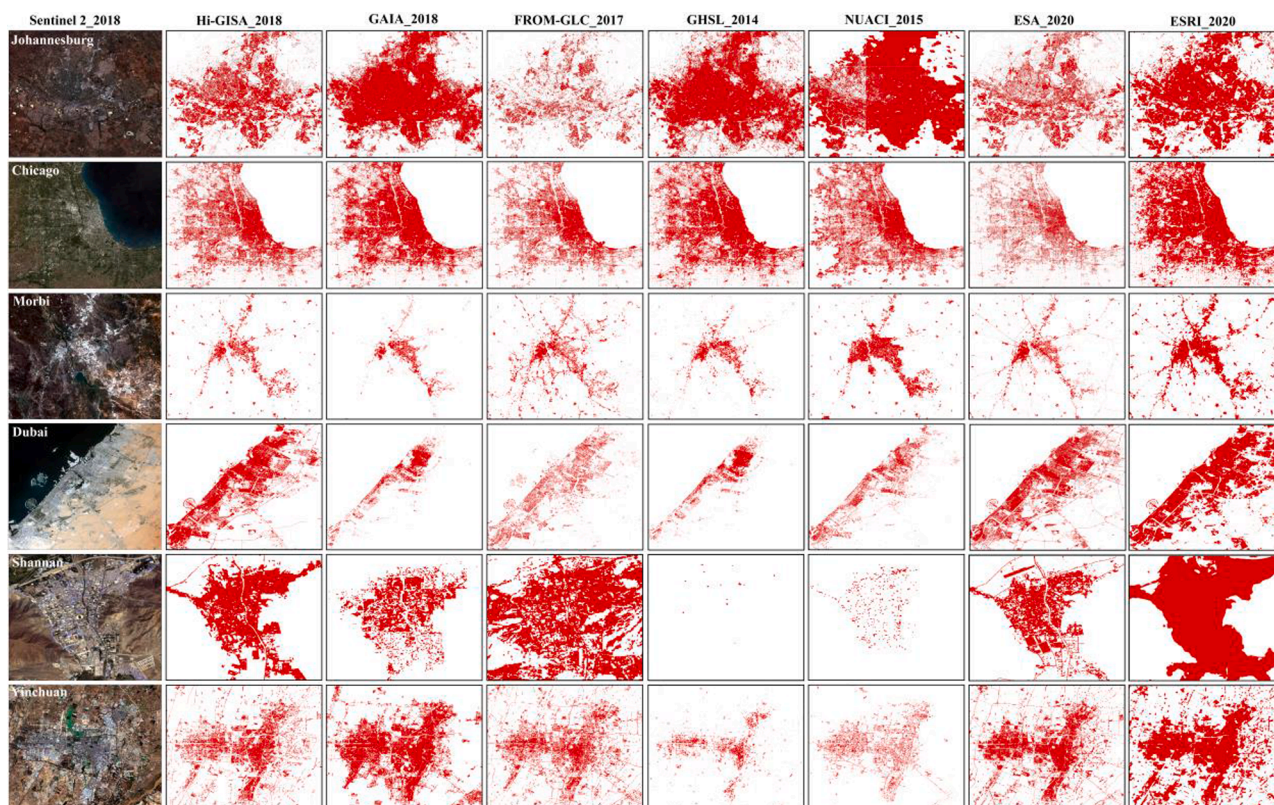
**Fig. 8.** Comparisons among different impervious surface maps derived from Hi-GISA and other products and procedures, including GAIA, FROM-GLC, GHSL, NUACI, ESA-WorldCover (https://esa-worldcover.org/en), and ESRI Land Cover (https://livingatlas.arcgis.com/landcover/) for six representative human settlements with various landscapes. The Sentinel-2 images were acquired and illustrated in true color with the GEE platform.
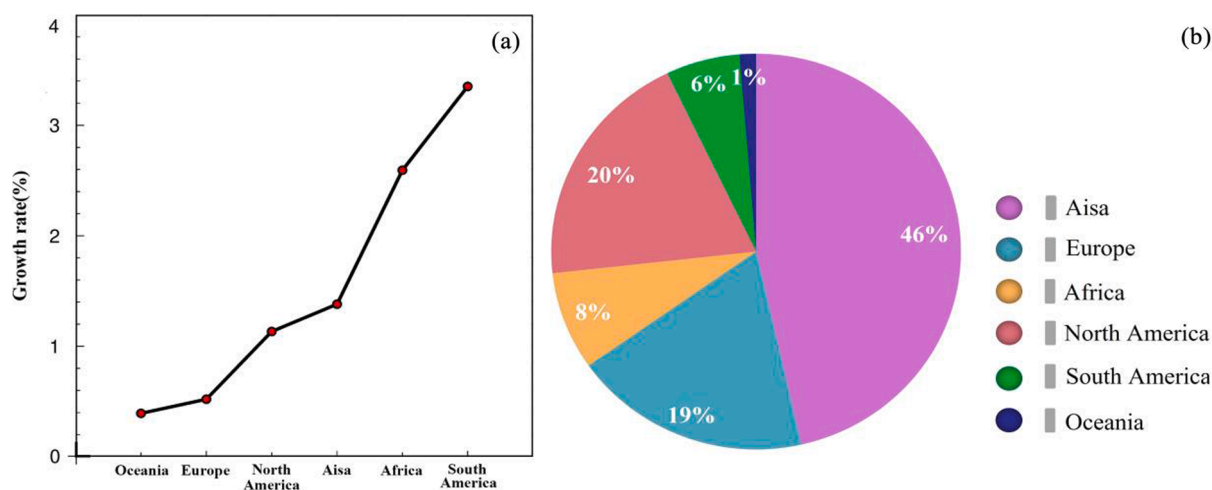


**Fig. 9.** Growth rates during the period 2015–2018 and the latest fractions of global total at the continental scale.

2018 with an increase of ~ 10,000 km$^2$. In total, the impervious surfaces derived from Hi-GISA was 1,285,179 km$^2$ in 2018, showing a continuous rise of ~ 20,000 km$^2$ from 2015. As a country with dramatic growth of impervious surfaces in recent years, the increased impervious surfaces in India had approached that in China between 2015 and 2018 (~3000 km$^2$). The largest contribution of impervious surface expansion came from China, India, USA, etc. The top 20 estimations of impervious surfaces for 2015 and 2018 at the national scale are shown in Fig. 10.

## 5. Discussion

### 5.1. Reliability and superiority of Hi-GISA

In this study, we developed an integrated approach to extract and update global impervious surfaces using all Sentinel images with the GEE platform. The effectiveness of utilizing a cloud computing platform and a threshold segmentation procedure to map human settlements across various landscapes was tested and confirmed. The Hi-GISA products show a superior temporal consistency that encourage the relevant application as baseline layers for globally comparative
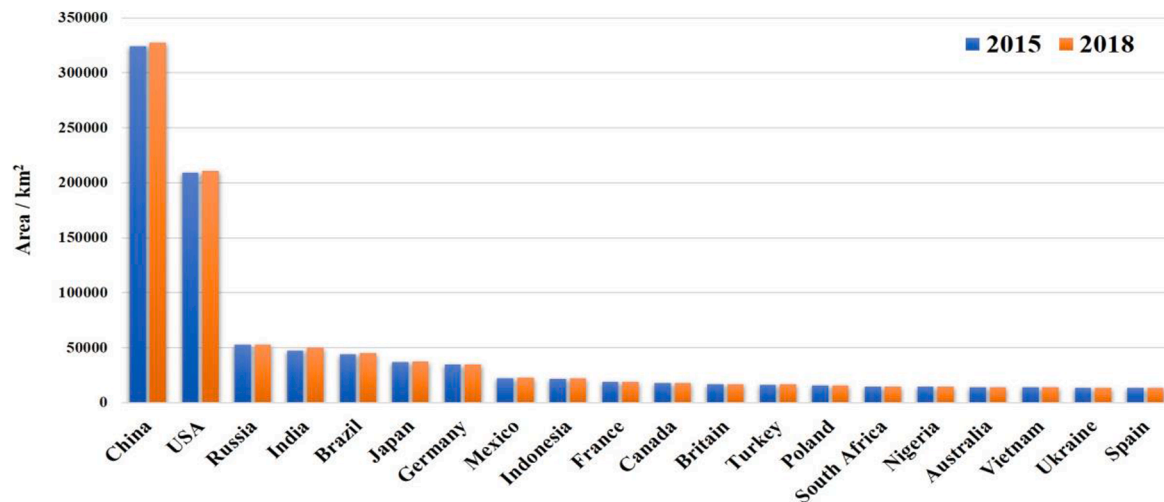
**Fig. 10.** The top 20 estimations of impervious surfaces for 2015 and 2018 at the national scale.

researches at a finer resolution.

With respect to improvements and advantages, Hi-GISA not only provided a spatially detailed delineation of human settlements in both urban and rural areas, but also offered quantitative change analyses for both expansion and reduction. According to the statistics derived from the Hi-GISA data, we identified three different trends: (1) Absolute expansion—there is only expansion and no reduction for the baseline impervious surface area; (2) Hybrid of expansion and reduction—expansion is accompanied by reduction; and (3) Absolute reduction only—existing impervious surfaces have been abandoned or demolished. For example, the Hi-GISA can accurately capture the areas that were demolished without newly built structures between 2015 and 2018. This ability makes our products more reliable for monitoring urban renewal process.

The average OA of Hi-GISA is >88% in both years. Although having a coverage of more impervious surfaces than others, Hi-GISA is consistent with contemporary global products at different spatial resolutions



**Fig. 11.** Comparisons of our high-resolution global impervious surface area (Hi-GISA) maps with several representative and reliable products developed during the period 2010–2020.

(Fig. 11). Gong et al. (2020) compared the contemporary datasets of impervious surface area using statistical aggregation and quantitative analyses. Similarly, we further carried out the comparison to facilitate the accuracy assessment for our products. In terms of total area, Hi-GISA is the closest to GlobeLand30 (Chen et al., 2015), which aggregates impervious surfaces occupying>1.2 million $km^2$, ~0.88% of the Earth's land surfaces. With respect to the total area for 2015 in China and USA, the Hi-GISA estimation approximate to those derived from China Land and Resources Bulletin (2016) and NLCD (2016), respectively, whereas GAIA (2018) and GHSL (2014) provide a much smaller statistic. The estimations from Hi-GISA and GlobeLand30 manifestly exceed the others due to the preservation of fine-scale human settlements. It is also worth mentioning that the total area of global impervious surfaces for 2020 was 0.43 million $km^2$ based on the ESA estimation, while this statistic could reach 1.41 million $km^2$ as per the ESRI estimation. Although it is difficult to compare different products, we might still conclude that the Hi-GISA data falls within a reasonable range of the mainstream datasets that are widely used in recent years. Furthermore, since we plan to produce global maps of impervious surface area from 2015 to 2030 at three-years intervals in support of monitoring and assessment of relevant SDG targets and indicators, the Hi-GISA maps can provide a baseline data source for analysis of global urban expansion when all the datasets are generated for the other years in the near future.

The Hi-GISA products with a resolution of 10 m can capture such artificial structures as small as cooling towers from thermal power plants or wind turbines. It was also found that the weathered landforms in limestone mountains or rocky outcrops in the desert might be identified as man-made objects wrongly. Here we adopted a thorough quality-improvement procedure to weed out these errors using visual interpretation, and this process can be highly automated with human interaction based on multisource ancillary data. More significantly, we employed the mode filtering method to clean up the edge noises and extract the temporal trend of impervious surfaces based on the SAR backscattering intensity change, which can facilitate the change detection quickly and data updating effectively on the premise of ensuring extraction accuracy. It is important to note that there is more to Hi-GISA than just identifying and delineating what is already represented in the similar datasets. For example, the Hi-GISA products clearly and accurately show large-area linear settlements along the coastal zones of Bangladesh and ridges of Northern Nairobi that are too small or dispersed to be extracted by most of the contemporary datasets as shown in Fig. 12.

### 5.2. Why Hi-GISA is better?

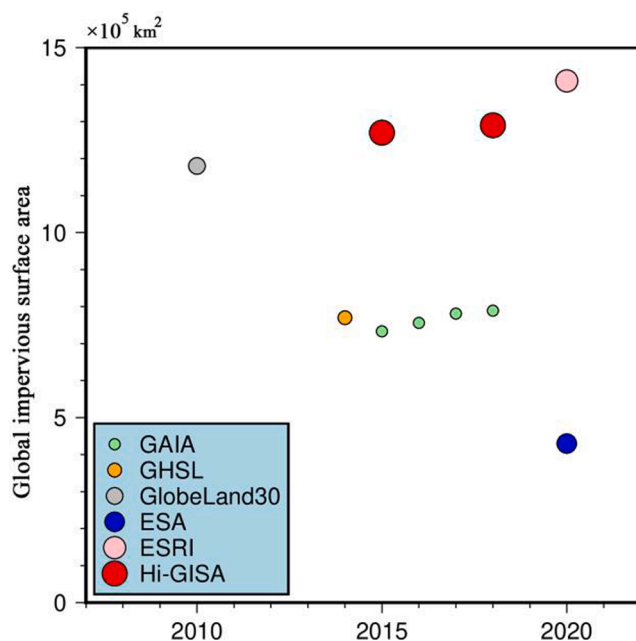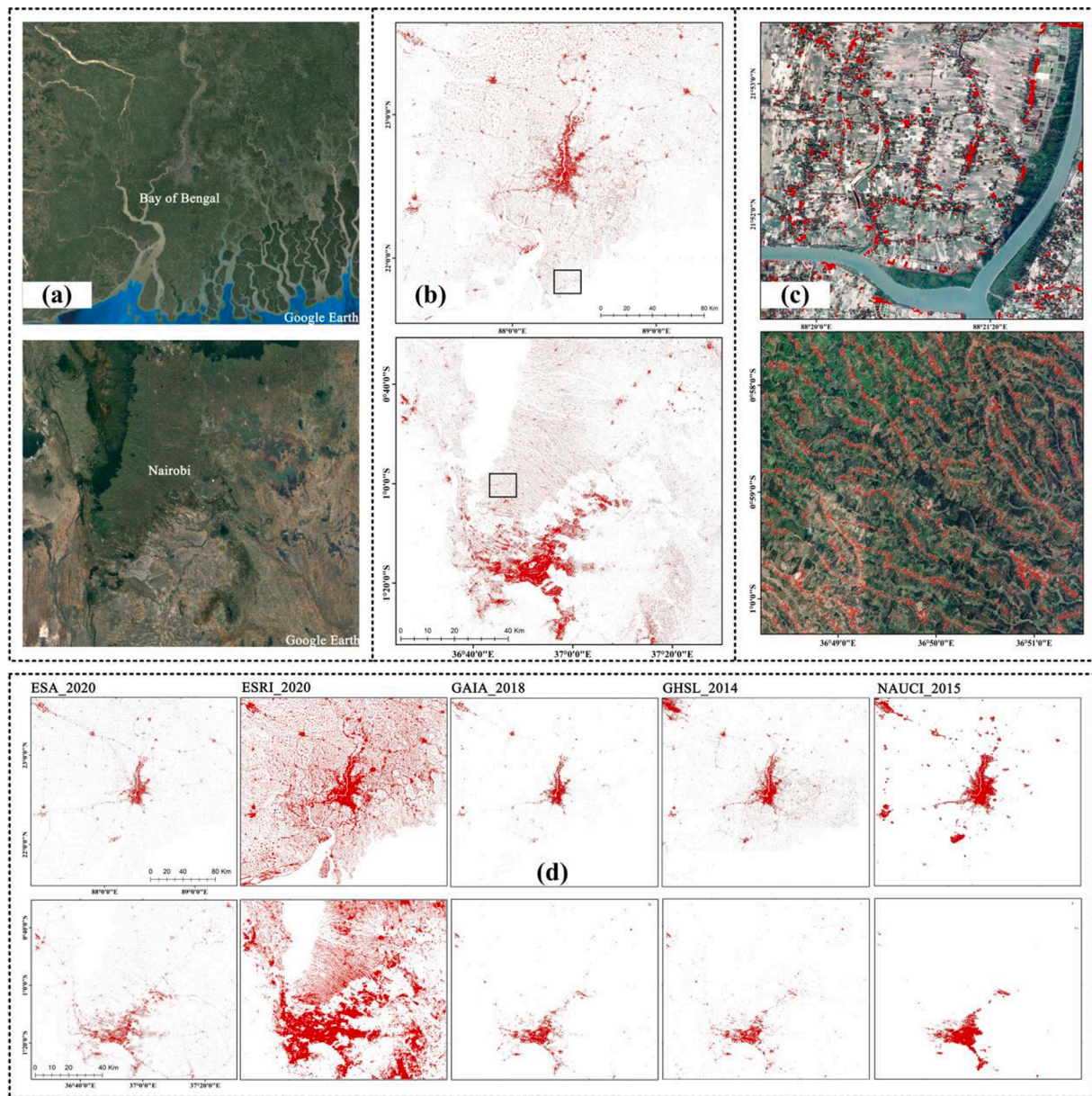Based on the big Earth data technology, the generation of Hi-GISA

**Fig. 12.** An example of the linear settlements along the coastal regions of Bangladesh and mountainous ridges of Northern Nairobi. (a) Google Earth images; (b) Spatial distributions of the Hi-GISA layers corresponding to satellite images; (c) Detailed overlay of Hi-GISA layer and satellite images referring to black-bordered boxes; (d) Spatial distributions of ESA, ESRI, GAIA, GHSL, and NAUCI layers in the same places.

data in this study fully used multi-temporal Sentinel-1 SAR images and Sentinel-2 optical images at 10 m resolution, and sufficiently considered the phenological characteristics of different ecological element layers covered by impervious surfaces according to finer-scale global biome maps. During the extraction process, we adopted appropriate empirical thresholds in a truly targeted and customized manner, and at the same time, we devoted meticulous visual interpretation efforts to fix false classifications when mapping the human settlements with complicated landscapes. To overcome the deficiencies of existing mainstream products, such as the relatively low accuracies in the middle and low latitudes and for arid and semi-arid areas, our Hi-GISA products had employed a semi-automatic procedure with intensive human interventions by referring to multisource ancillary data such as the NTL imagery and DEM topographic information. Additionally, we applied a thorough post-editing quality-improvement procedure to reduce commission errors and omission errors, and to preserve the fine-scale boundaries of varying human settlements through heavily manual

treatments. Thanks to the application of big Earth data technology and the usage of highly automated procedures with human interactions, the Hi-GISA data could thus have higher mapping accuracy for different types of human settlements with various landscapes in both urban and rural areas, and demonstrate a better fit with the reference data than other urban land cover products across different geographical regions.

### 5.3. Limitations and prospects of Hi-GISA

To our knowledge, there are some limitations in terms of data sources and processing approaches, although the proposed procedure shows the capability to extract accurate impervious surface area at the global scale. In mid-low latitude zones and arid regions, the representation of impervious surface area utilizing the SAR-based Hi-GISA technique differs significantly from the impervious surface area mapping solely based on optical remote sensing data. The artificial structures such as asphalt highways and manufacturing sheds might not be

classified as impervious surfaces in the Hi-GISA layers. We therewith used spectral indices based on optical images together with the Open Street Map (OSM) data to supplement the identification of airport runways and narrow roads in sparsely populated areas, although some omissions might remain. The results of accuracy assessment indicated that omission errors occurred more frequently in sparsely populated regions (e.g., scattered rural settlements) than in heavily populated urban agglomerations (modern metropolises like Beijing, Shanghai, Chicago, New York, Los Angeles, etc.). Therefore, future direction will target at the omission in sparsely populated regions by using higher resolution images. Besides, the Hi-GISA data can be applied to meet the data needs of SDG indicator 11.3.1 and serve as a high-quality sample library for human settlement machine learning to achieve fully automated extraction of impervious surfaces worldwide.

## 6. Conclusions

By using the Sentinel data including SAR and optical images within the GEE cloud computing platform, we created spatially explicit and temporally consistent global maps of impervious surface area at 10-m spatial resolution for 2015 and 2018, namely the high-resolution global impervious surface area (Hi-GISA) maps. It has been manifested that the big Earth data technologies can help to generate a more accurate product of global human settlement distribution. During the extraction and updating processes, we elaborately selected relevant features to suppress background information, which greatly improved the extraction accuracy and enhanced the updating efficiency for human settlements with various landscapes in both urban and rural areas. The relevant research has shown that such Hi-GISA data products can be utilized for analysis of urban expansion at the city level (Jiang et al., 2021a and 2021b). In addition, the Hi-GISA data can be potentially useful to examine urban sprawl (Bhatta et al., 2010; Cieślak et al., 2020) for estimating urban heat islands (Zhou et al., 2018; Chakraborty et al., 2020) and for integration with weather and climate models (Bontemps et al., 2013).

The Hi-GISA products are reliable as demonstrated by the validation with randomly selected blocks and comparison with contemporary global products of impervious surface area. The average OA of Hi-GISA is>88% for each period. The cross-product comparison shows that the Hi-GISA data does accord with the reasonable range in terms of aggregation statistics. In addition, the improved procedure can identify and preserve more spatial details, especially for small and scattered human settlements. Based on the aggregation results derived from Hi-GISA, a continuous and steady growth in global impervious surfaces has been substantiated between 2015 and 2018. The total area of global impervious surfaces grew from 1.27 million $km^2$ in 2015 to 1.29 million $km^2$ in 2018 with an increase of 20,000 $km^2$. South America showed the greatest growth (~3.35%) among continents, followed by Africa (~2.59%). China, USA, and Russia collectively accounted for ~ 50% of the global impervious surfaces in 2018, and there are only 2 countries from Africa among the top 20 countries, namely Nigeria and South Africa.

In summary, the Hi-GISA maps can provide finer human settlement footprint and preliminary semantic information about anthropogenic environment to satisfy the monitoring and assessment requirements of SDG 11 related indicators. Meanwhile, this dataset can also portray the spatiotemporal evolution of urban–rural human settlement expansion, which will serve as a high-quality benchmark for urbanization sustainability assessment.

## CRediT authorship contribution statement

**Zhongchang Sun:** Conceptualization, Data curation, Validation, Methodology, Writing – original draft. **Wenjie Du:** Data curation, Methodology, Writing – original draft. **Huiping Jiang:** Data curation, Validation, Methodology, Writing – original draft, Writing – review &

editing. **Qihao Weng:** Writing – review & editing, Supervision. **Huadong Guo:** Conceptualization, Supervision. **Youmei Han:** Data curation, Validation. **Qiang Xing:** Writing – review & editing. **Yuanxu Ma:** Supervision.

## Declaration of Competing Interest

The authors declare that they have no known competing financial interests or personal relationships that could have appeared to influence the work reported in this paper.

## References

Ban, Y., Jacob, A., Gamba, P., 2015. Spaceborne SAR data for global urban mapping at 30m resolution using a robust urban extractor. ISPRS J. Photogramm. Remote Sens. 103, 28–37.

Bhatta, B., Saraswati, S., Bandyopadhyay, D., 2010. Urban sprawl measurement from remote sensing data. Appl. Geogr. 30 (4), 731–740. https://doi.org/10.1016/j.apgeog.2010.02.002.

Bontemps, S., Defourny, P., Radoux, J., Van Bogaert, E., Lamarche, C., Achard, F., Mayaux P., Boettcher M., Brockmann C., Kirches G., Zülkhe M., Kalogirou V., Seifert F.M., Arino O., 2013. Consistent global land cover maps for climate modelling communities: current achievements of the ESA's land cover CCI. Paper presented at the Proceedings of the ESA living planet symposium, Edimburgh. Available from https://ftp.space.dtu.dk/pub/Ioana/papers/s274_2bont.pdf.

Cao, W., Zhou, Y., Li, R., Li, X., 2020. Mapping changes in coastlines and tidal flats in developing islands using the full time series of Landsat images. Remote Sens. Environ. 239, 111665. https://doi.org/10.1016/j.rse.2020.111665.

Chakraborty, T., Hsu, A., Manya, D., Sheriff, G., 2020. A spatially explicit surface urban heat island database for the United States: Characterization, uncertainties, and possible applications. ISPRS J. Photogramm. Remote Sens. 168, 74–88. https://doi.org/10.1016/j.isprsjprs.2020.07.021.

Chen, J., Chen, J., Liao, A., Cao, X., Chen, L., Chen, X., He, C., Han, G., Peng, S., Lu, M., Zhang, W., Tong, X., Mills, J., 2015. Global land cover mapping at 30 m resolution: A POK-based operational approach. ISPRS J. Photogramm. Remote Sens. 103, 7–27. https://doi.org/10.1016/j.isprsjprs.2014.09.002.

Chen, J., Cihlar, J., 1996. Retrieving leaf area index of boreal conifer forests using Landsat TM images. R Remote Sens. Environ. 55 (2), 153–162. https://doi.org/10.1016/0034-4257(95)00195-6.

Cieślak, I., Biłozor, A., Szuniewicz, K., 2020. The use of the CORINE Land Cover (CLC) database for analyzing urban sprawl. Remote Sens. 12 (2), 282. https://doi.org/10.3390/rs12020282.

Civco, D., Hurd, J.D., Wilson, E.H., Arnold, C.L., Prisloe, M.P., 2002. Quantifying and describing urbanizing landscapes in the northeast United States. Photogramm. Eng. Remote Sens. 68, 1083–1090.

Corbane, C., Pesaresi, M., Kemper, T., Politis, P., Florczyk, A.J., Syrris, V., Melchiorri, M., Sabo, F., Soille, P., 2019. Automated global delineation of human settlements from 40 years of Landsat satellite data archives. Big Earth Data. 3(2), 140–69, https://doi.org/10.1080/20964471.2019.1625528.

Deng, C., Wu, C., 2012. BCI: A biophysical composition index for remote sensing of urban environments. Remote Sens. Environ. 127, 247–259. https://doi.org/10.1016/j.rse.2012.09.009.

Esch, T., Marconcini, M., Felbier, A., Roth, A., Heldens, W., Huber, M., Schwinger, M., Taubenböck, H., Müller, A., Dech, S., 2013. Urban footprint processor—fully automated processing chain generating settlement masks from global data of the TanDEM-X mission. IEEE Geosci. Remote Sens. Lett. 10 (6), 1617–1621. https://doi.org/10.1109/lgrs.2013.2272953.

Esch, T., Thiel, M., Schenk, A., Roth, A., Muller, A., Dech, S., 2010. Delineation of Urban Footprints from TerraSAR-X Data by Analyzing Speckle Characteristics and Intensity Information. IEEE Trans. Geosci. Remote Sens. 48 (2), 905–916. https://doi:10.1109/tgrs.2009.2037144.

Esch, T., Heldens, W., Hirner, A., Keil, M., Marconcini, M., Roth, A., Zeidler, J., Dech, S., Strano, E., 2017. Breaking new ground in mapping human settlements from space – The Global Urban Footprint. ISPRS J. Photogramm. Remote Sens. 134, 30–42. https://doi.org/10.1016/j.isprsjprs.2017.10.012.

Ge, Y., Hu, S., Ren, Z., Jia, Y., Wang, J., Liu, M., Zhang, D., Zhao, W., Luo, Y., Fu, Y., Bai, H., Chen, Y., 2019. Mapping annual land use changes in China's poverty-stricken areas from 2013 to 2018. Remote Sens. Environ. 232, 111285. https://doi.org/10.1016/j.rse.2019.111285.

Gong, P., Liu, H., Zhang, M., Li, C., Wang, J., Huang, H., Clinton, N., Ji, L., Li, W., Bai, Y., Chen, B., Xu, B., Zhu, Z., Yuan, C., Ping Suen, H., Guo, J., Xu, N., Li, W., Zhao, Y., Yang, J., Yu, C., Wang, X.i., Fu, H., Yu, L.e., Dronova, I., Hui, F., Cheng, X., Shi, X.,

Xiao, F., Liu, Q., Song, L., 2019. Stable classification with limited sample: transferring a 30-m resolution sample set collected in 2015 to mapping 10-m resolution global land cover in 2017. Sci. Bull 64 (6), 370–373. https://doi.org/10.1016/j.scib.2019.03.002.

Gong, P., Li, X., Wang, J., Bai, Y., Chen, B., Hu, T., Liu, X., Xu, B., Yang, J., Zhang, W., Zhou, Y., 2020. Annual maps of global artificial impervious area (GAIA) between 1985 and 2018. Remote Sens. Environ. 236, 111510. https://doi.org/10.1016/j.rse.2019.111510.

Guo, H., 2017. Big Earth data: A new frontier in Earth and information sciences. Big Earth Data. 1 (1–2), 4–20. https://doi.org/10.1080/20964471.2017.1403062.

Guo, H., Nativi, S., Liang, D., Craglia, M., Wang, L., Schade, S., Corban, C., He, G., Pesaresi, M., Li, J., Shirazi, Z., Liu, J., Annoni, A., 2020. Big Earth Data science: an information framework for a sustainable planet. Int. J. Digit. Earth. 13 (7), 743–767. https://doi.org/10.1080/17538947.2020.1743785.

Huang, X., Li, J., Yang, J., Zhang, Z., Li, D., Liu, X., 2021. 30 m global impervious surface area dynamics and urban expansion pattern observed by Landsat satellites: From 1972 to 2019. Sci. China Earth Sci. 64 (11), 1922–1933. https://doi.org/10.1007/s11430-020-9797-9.

Jiang, H., Sun, Z., Guo, H., Weng, Q., Du, W., Xing, Q., Cai, G., 2021a. An assessment of urbanization sustainability in China between 1990 and 2015 using land use efficiency indicators. npj Urban Sustainability. 1 (1), 1–13. https://doi.org/10.1038/s42949-021-00032-y.

Jiang, H., Sun, Z., Guo, H., Xing, Q., Du, W., Cai, G., 2021b. A standardized dataset of built-up areas of China's cities with populations over 300,000 for the period 1990–2015. Big Earth Data. 6 (1), 103–126. https://doi.org/10.1080/20964471.2021.1950351.

Li, G., Lu, D., Moran, E., Hetrick, S., 2013. Mapping impervious surface area in the Brazilian Amazon using Landsat Imagery. GISci. Remote Sens. 50, 172–183. https://doi:10.1080/15481603.2013.780452.

Liu, C., Shao, Z., Chen, M., Luo, H., 2013. MNDISI: A multi-source composition index for impervious surface area estimation at the individual city scale. Remote Sens. Lett. 4 (8), 803–812.

Liu, X., Hu, G., Chen, Y., Li, X., Xu, X., Li, S., Pei, F., Wang, S., 2018. High-resolution multi-temporal mapping of global urban land using Landsat images based on the Google Earth Platform. Remote Sens. Environ. 209, 227–239. https://doi.org/10.1016/j.rse.2018.02.055.

Liu, X., Huang, Y., Xu, X., Li, X., Li, X., Ciais, P., Lin, P., Gong, K., Ziegler, A., Chen, A., Gong, P., Chen, J., Hu, G., Chen, Y., Wang, S., Wu, Q., Huang, K., Estes, L., Zeng, Z., 2020. High-spatiotemporal-resolution mapping of global urban change from 1985 to 2015. Nature Sustainability. 3(7), 564–570, https://doi.org/10.1038/s41893-020-0521-x.

Lu, D., Weng, Q., 2004. Spectral mixture analysis of the urban landscape in Indianapolis with Landsat ETM plus imagery. Photogramm. Eng. Remote Sens. 70, 1053–1062. https://doi.org/10.14358/PERS.70.9.1053.

Lu, D., Li, G., Kuang, W., Moran, E., 2014. Methods to extract impervious surface areas from satellite images. Int. J. Digit. Earth. 7, 93–112. https://doi:10.1080/17538947.2013.866173.

McFeeters, S., 1996. The use of the Normalized Difference Water Index (NDWI) in the delineation of open water features. Int. J. Remote Sens. 17 (7), 1425–1432. https://doi.org/10.1080/01431169608948714.

Olson, D., Dinerstein, E., Wikramanayake, E., Burgess, N., Powell, G., Underwood, E., D'amico, J., Itoua, I., Strand, H., Morrison, J., Loucks, C., Allnutt, T., Ricketts, T., Kura, Y., Lamoreux, J., Wettengel, W., Hedao, P., Kassem, K., 2001. Terrestrial Ecoregions of the World: A New Map of Life on Earth. Bioscience 51 (11), 933–938. https://doi.org/10.1641/0006-3568(2001)051[0933:TEOTWA]2.0.CO;2.

Pesaresi, M., Huadong, G., Blaes, X., Ehrlich, D., Ferri, S., Gueguen, L., Halkia, M., Kauffmann, M., Kemper, T., Lu, L., Marin-Herrera, M.A., Ouzounis, G.K., Scavazzon, M., Soille, P., Syrris, V., Zanchetta, L., 2013. A global human settlement layer from optical HR/VHR RS data: concept and first results. IEEE J. Sel. Top. Appl. Earth Obs. Remote Sens. 6 (5), 2102–2131.

Shao, Y., Li, G., Guenther, E., Campbell, J.B., 2015. Evaluation of Topographic Correction on Subpixel Impervious Cover Mapping With CBERS-2B Data. IEEE Geosci. Remote Sens. Lett. 12, 1–5. https://doi.org/10.1109/lgrs.2015.2419135.

Schneider, A., Friedl, M.A., Potere, D., 2010. Mapping global urban areas using MODIS 500-m data: New methods and datasets based on 'urban ecoregions'. Remote Sens. Environ. 114 (8), 1733–1746. https://doi.org/10.1016/j.rse.2010.03.003.

Sun, Z., Xu, R., Du, W., Wang, L., Lu, D., 2019. High-resolution urban land mapping in China from Sentinel 1A/2 imagery based on Google Earth Engine. Remote Sens. 11, 752. https://doi.org/10.3390/rs11070752.

Thomas, E., Erik, A., Niki, F., Timon, M., Per, O., Owen, G., Kazuhiko, T., Carl, F., 2019. Sustainability and resilience for transformation in the urban century. Nature Sustainability. 2: 267–273, https:// doi.org/10.1038/s41893-019-0250-1.

United Nations, Department of Economic and Social Affairs, Population Division, 2018. World Urbanization Prospects: The 2018 Revision. Online Edition, Available from https://esa.un.org/unpd/wup/Publications.

United Nations, 2017. The Sustainable Development Goals Report 2017. Online Edition, Available from https://unstats.un.org/sdgs/report/2017/.

United Nations, 2015. Transforming our World: the 2030 Agenda for Sustainable Development. http://www.un.org/ga/search/view_doc.asp?symbol=A/RES/70/1&Lang= E.

UN-Habitat, 2019. A guide to assist national and local governments to monitor and report on SDG goal 11+ indicators, Online Edition. Available from https://www.localizingthesdgs.org/library/60/SDG-Goal-11-Monitoring-Framework-A-guide-to-assist-national-and-local-governments-to-monitor-and-report-on-SDG-goal-11-indicators.pdf.

Wang, Y., Ziv, G., Adami, M., Mitchard, E., Batterman, S.A., Buermann, W., Schwantes Marimon, B., Marimon Junior, B.H., Matias Reis, S., Rodrigues, D., Galbraith, D., 2019. Mapping tropical disturbed forests using multi-decadal 30 m optical satellite imagery. Remote Sens. Environ. 221, 474–488. https://doi.org/10.1016/j.rse.2018.11.028.

Wang, Z., Gang, C., Li, X., Chen, Y., Li, J., 2015. Application of a normalized difference impervious index (NDII) to extract urban impervious surface features based on Landsat TM images. Int. J. Remote Sens. 36, 1–15. https://doi.org/10.1080/01431161.2015.1007250.

Weng, Q., 2012. Remote sensing of impervious surfaces in the urban areas: Requirements, methods, and trends. Remote Sens. Environ. 117, 34–49. https://doi.org/10.1016/j.rse.2011.02.030.

Weng, Q., Hu, X., 2008. Medium spatial resolution satellite imagery for estimating and mapping urban impervious surfaces using LSMA and ANN. IEEE Trans. Geosci. Remote Sens. 46, 2397–2406. https://doi.org/10.1109/tgrs.2008.917601.

Wu, M., Zhao, X., Sun, Z., Guo, H., 2019. A hierarchical multiscale super-pixel-based classification method for extracting urban impervious surface using Deep Residual Network from WorldView-2 and LiDAR data. IEEE J. Sel. Top. Appl. Earth Obs. Remote Sens. 12 (1), 210–222.

Wu, C., Murray, A.T., 2003. Estimating impervious surface distribution by spectral mixture analysis. Remote Sens. Environ. 84, 493–505. https://doi:10.1016/s0034-4257(02)00136-0.

Xian, G., Homer, C., 2010. Updating the 2001 national land cover database impervious surface products to 2006 using Landsat imagery change detection methods. Remote Sens. Environ. 114 (8), 1676–1686. https://doi.org/10.1016/j.rse.2010.02.018.

Xu, H., 2010. Analysis of Impervious Surface and its Impact on Urban Heat Environment using the Normalized Difference Impervious Surface Index (NDISI). Photogramm. Eng. Remote Sens. 76, 557–565. https://doi.org/10.14358/pers.76.5.557.

Yang, J., Huang, X., 2021. The 30 m annual land cover dataset and its dynamics in China from 1990 to 2019. Earth Syst. Sci. Data. 13 (8), 3907–3925. https://doi.org/10.5194/essd-13-3907-2021.

Yang, L., Huang, C., Homer, C., Wylie, B., Coan, M., 2003. An approach for mapping large-area impervious surfaces: Synergistic use of Landsat-7 ETM+ and high spatial resolution imagery. Can. J. Remote Sens. 29, 230–240. https://doi:10.5589/m02-098.

Zhang, Q., Schaaf, C., Seto, K.C., 2013. The vegetation adjusted NTL urban index: A new approach to reduce saturation and increase variation in nighttime luminosity. Remote Sens. Environ. 129, 32–41. https://doi.org/10.1016/j.rse.2012.10.022.

Zhang, Y., Zhang, H., Lin, H., 2014. Improving the impervious surface estimation with combined use of optical and SAR remote sensing images. Remote Sens. Environ. 141, 155–167. https://doi.org/10.1016/j.rse.2013.10.028.

Zhang, C., Sargent, I., Pan, X., Li, H., Gardiner, A., Hare, J., Atkinson, P.M., 2018. An object-based convolutional neural network (OCNN) for urban land use classification. Remote Sens. Environ. 216, 57–70. https://doi.org/10.1016/j.rse.2018.06.034.

Zhang, X., Liu, L., Wu, C., Chen, X., Gao, Y., Xie, S., Zhang, B., 2020. Development of a global 30 m impervious surface map using multisource and multitemporal remote sensing datasets with the Google Earth Engine platform. Earth Syst. Sci. Data 12, 1625–1648. https://doi.org/10.5194/essd-12-1625-2020.

Zhou, D., Xiao, J., Bonafoni, S., Berger, C., Deilami, K., Zhou, Y., Frolking, S., Yao, R., Qiao, Z., Sobrino, J., 2018. Satellite remote sensing of surface urban heat islands: Progress, challenges, and perspectives. Remote Sens. 11 (1), 48. https://doi.org/10.3390/rs11010048.

## Further reading

Goldblatt, R., You, W., Hanson, G., Khandelwal, A.K., 2016. Detecting the boundaries of urban areas in India: A dataset for pixel-based image classification in Google Earth Engine. Remote Sens. 8, 634. https://doi.org/10.3390/rs8080634.

Li, X., Gong, P., Liang, L., 2015. A 30-year (1984–2013) record of annual urban dynamics of Beijing City derived from Landsat data. Remote Sens. Environ. 166, 78–90. https://doi.org/10.1016/j.rse.2015.06.007.